



<http://www.diva-portal.org>

This is the published version of a paper published in *Advanced Engineering Materials*.

Citation for the original published paper (version of record):

Lin, Z., Surreddi, K B., Hulme-Smith, C., Dadbakhsh, S., Rashid, A. (2023)
Influence of PBF#EB process Parameters on Transformation Temperatures and
Pseudoelasticity of Shape Memory Nickel Titanium
Advanced Engineering Materials
<https://doi.org/10.1002/adem.202201818>

Access to the published version may require subscription.

N.B. When citing this work, cite the original published paper.

Permanent link to this version:

<http://urn.kb.se/resolve?urn=urn:nbn:se:kth:diva-326103>

Influence of Electron Beam Powder Bed Fusion Process Parameters on Transformation Temperatures and Pseudoelasticity of Shape Memory Nickel Titanium

Zeyu Lin,^{*} Kumar Babu Surreddi, Christopher Hulme, Sasan Dadbakhsh, and Amir Rashid

Electron beam powder bed fusion (PBF-EB) is used to manufacture dense nickel titanium parts using various parameter sets, including the beam current, scan speed, and postcooling condition. The density of manufactured NiTi parts is investigated in relation to the linear energy input. The results imply that the part density increases with increasing linear energy density to over 98% of the bulk density. With a constant energy input, a combination of low power and low scan speed leads to denser parts. This is attributed to lower electrostatic repulsive forces from lower number density of the impacting electrons. After manufacturing, the densest parts with distinct parameter sets are categorized into three groups: 1) high power with high scan speed and vacuum slow cooling, 2) low power with low scan speed and vacuum slow cooling, and 3) low power with low scan speed and medium cooling rate in helium gas. Among these, a faster cooling rate suppresses phase transformation temperatures, while vacuum cooling combinations do not affect the phase transformation temperatures significantly. Herein, all the printed parts exhibit almost 8% pseudoelasticity regardless of the process parameters, while the parts cooled in helium have a higher energy dissipation efficiency ($1 - \eta$), which implies faster damping of oscillations.

1. Introduction

Nickel titanium (NiTi) is one of the most utilized shape memory alloys. It has, therefore, drawn significant attention and interest due to its unique characteristics, such as the shape memory effect and pseudoelasticity/superelasticity.^[1] In addition to these functional features, superior mechanical properties, excellent biocompatibility, and cyclic stability expanded the application of NiTi in different industries, including aerospace, biomedical, automotive, and actuators.^[2,3] The shape memory and pseudoelasticity properties of NiTi are based on a solid–solid reversible martensitic phase transformation between low-temperature monoclinic martensite (B19' structure) and high-temperature cubic austenite (B2 structure).^[4] Above the austenite transformation finish temperature (A_f), the martensitic phase can be induced by applying stress to achieve plastic deformation without generating dislocations.


After unloading, the martensite reverts back to austenite, causing it to regain its original shape.^[5] During both unloading and heating, shape memory effect and pseudoelasticity/superelasticity properties can typically restore strains up to around 8% in NiTi.^[2] In addition to this, the high damping capacity (i.e., material ability to dissipate elastic strain energy during mechanical vibration or wave propagation) of the martensitic NiTi is associated with the hysteretic transition between the twinned martensite variants or different phase interfaces. Moreover, the damping capacity of NiTi increases with increasing amplitude of the applied vibration.^[6] This leads to a long fatigue life and a stable resistance of large amplitude of vibration, which makes NiTi a good candidate for tool holders in machining processes.^[7]

Owing to NiTi mechanical properties, it is very difficult to conventionally machine this material.^[8] This necessitates other methods in fabricating NiTi devices, such as casting and powder metallurgy. Casting has been the most common method to date, which is often associated with the formation of impurities (e.g., TiC, $Ti_4Ni_2O_x$) due to the high-processing temperature, while difficulties associated with postcasting machining are another hindrance to spreading this method. Powder metallurgy is also limited in the complexity of the parts and achieving the

Z. Lin, S. Dadbakhsh, A. Rashid
Department of Production Engineering
KTH Royal Institute of Technology
Brinellvägen 68, SE-114 28 Stockholm, Sweden
E-mail: zeyul@kth.se

K. B. Surreddi
Materials Technology
School of Information and Technology
Dalarna University
SE-791 88 Falun, Sweden

C. Hulme
Department of Materials Science and Engineering
KTH Royal Institute of Technology
SE-100 44 Stockholm, Sweden

 The ORCID identification number(s) for the author(s) of this article can be found under <https://doi.org/10.1002/adem.202201818>.

© 2023 The Authors. Advanced Engineering Materials published by Wiley-VCH GmbH. This is an open access article under the terms of the Creative Commons Attribution-NonCommercial-NoDerivs License, which permits use and distribution in any medium, provided the original work is properly cited, the use is non-commercial and no modifications or adaptations are made.

DOI: 10.1002/adem.202201818

demanding shape and size requirements of the porosity in the biomedical industry.^[1,2,9] In recent years, researchers have focused on additive manufacturing (AM) as an alternative and modern technique to process NiTi parts due to its capability of manufacturing complex geometries and to minimize postmachining. So far, laser-based AM processes have been used to explore the possibilities to fabricate NiTi parts. For example, Dadbakhsh et al.^[10] have worked on laser powder bed fusion (PBF-LB) of NiTi, leading to a single transformation in differential scanning calorimetry (DSC) curves of as-built parts while there were some serrations from potential chemical inhomogeneity in the curves corresponding to the starting powder. Low-power, low-speed parameters led to a prominent thermal memory response due to the stability of the martensite at room temperature while parts fabricated with high-power, high-speed parameters exhibited a pseudoelasticity because the austenitic phase dominates at room temperature. Furthermore, Speirs et al.^[11] revealed that the martensite start temperature decreases with increasing laser scanning speed in PBF-LB process. Since the high laser speed can reduce the size of precipitates formed in the matrix or even suppress them completely with respect to the PBF-LB atmospheric (with oxygen and nitrogen), which form oxides or nitrides to influence the Ni-concentration in the matrix.

In comparison to PBF-LB, electron beam powder bed fusion (PBF-EB), also known as selective electron beam melting (SEBM) or electron beam melting (EBM) is carried out in a vacuum chamber, which can effectively prevent contamination by oxygen and nitrogen, ensuring the chemical purity. The preheating process keeps both the baseplate and powder bed at a constant high temperature, which can relieve the residual stress and generate a more homogenous microstructure.^[12] Nevertheless, PBF-EB could be still a very challenging process for NiTi, partly due to the high risk of smoke during the preheating stage. Smoking is the sudden spatter of the powders mainly because of the repulsive electron static charges. This is particularly high for NiTi powder due to the passive titanium oxide film on the surfaces which hinders the dissipation of the electrons.^[13] Therefore, up to now, there are only very few successful attempts on manufacturing NiTi using PBF-EB. The first attempt was reported by Muhammad et al.^[14] who failed to observe shape memory or pseudoplasticity effect on the as-built part due to the formation of unwanted phases, for instance, Ni₂Ti and Ni₃Ti. In contrast, Zhou et al.^[15] have reported as-printed samples with excellent pseudoplasticity at room temperature through a two-step phase transformation during cooling and one-step transformation during heating. Following that, most recently Ren et al.^[16] have investigated the influence of PBF-EB parameters (e.g., focus offset, speed function) on the properties of NiTi parts. They found that both focus offset and speed function have a minor influence on the as-built part properties, such as phase constitution, phase transformation, and microhardness. However, the defects introduced by using a higher focus offset and higher speed function affected the mechanical properties. This was due to the fact that higher focus offset and speed function value decrease the input energy density, which resulted in manufacturing defects. Moreover, Wang et al.^[17] carried out NiTi in situ alloying by synthesizing elemental Ni and Ti powder within PBF-EB at different preheating

temperatures. They found that the self-sustaining high-temperature synthesis (SHS) was ignited using a preheating at 450 and 600 °C. In contrast, preheating to 350 °C was not sufficient to sinter the newly laid elemental powder, resulting in porous samples. Nevertheless, the uncontrolled combustion at higher temperature and the lack of fusion at lower preheating temperatures make the PBF-EB of premixed Ni-Ti powders to be a problematic practice.

Furthermore, some research works have investigated the dimensional accuracy of PBF-EB parts in relation to the process parameters for other alloys such as Inconel 718. Accordingly, the dimensional accuracy of the samples without contouring is higher than those made with one due to the excess energy input which leads to a bigger dimension for the final part.^[18] In addition, input energy density can influence the dimensional accuracy, as the inaccuracy is considerably decreased by decreasing the energy. This also mitigates “peeling up” which is the distortion of the material above the final layer during the build.^[19]

Although PBF-EB operates at a high temperature, there is no literature reporting the effect of postcooling rate on the final part of PBF-EB. The postcooling rate could also be a crucial parameter for highly sensitive NiTi. Also, the correlation between the process parameters and the geometrical outcome is rather neglected as well. Accordingly, in this research, various processing-related PBF-EB parameters including postcooling rate were used to demonstrate their interconnected correspondence on the geometrical mismatch and the phase transformation and mechanical properties of the NiTi parts.

2. Experimental Section

Prealloyed NiTi powder (nominal Ni content of 50.6 at%) was produced using gas atomization with argon gas to produce a powder size with the distribution of $45 \leq d/\mu\text{m} < 105$ and $d_{50} \approx 70 \mu\text{m}$. The morphology of the powder particle was spherical (TLS Technik GmbH & Co). A PBF-EB Arcam A2X machine from Arcam AB (GE additive, Sweden) was utilized for the additive manufacturing of NiTi parts. To reduce the required powder volume, a smaller in-house retrofitted build platform with a build volume of $100 \times 100 \times 150 \text{ mm}^3$ was used. The automation mode was turned off and the manual mode was used to perform the entire experiment. Density cubes with a size of $10 \times 10 \times 10 \text{ mm}^3$ were manufactured on a stainless steel baseplate with a size of $75 \times 75 \times 10 \text{ mm}^3$ in each build. The distance between cubes was over 10 mm to reduce the thermal influence from neighboring cubes, as shown in **Figure 1a**. The layer thickness was set to 75 μm and the working temperature was 750 °C. During the process, each new powder layer was leveled and preheated to the working temperature to prevent smoking. The focus offset for the melting theme was 0 mA for all the samples and the beam current and scan speed were set, as shown in **Table 1**. No contour was printed and the scan strategy for the hatching area was set to snake mode (i.e., bidirectional scanning pattern) with a line offset of 0.125 mm. There were three batches, which generate a total of 13 density cubes. The entire process time for each built was around 2 h. In addition, there are two different cooling modes for this machine shown in **Figure 2**.

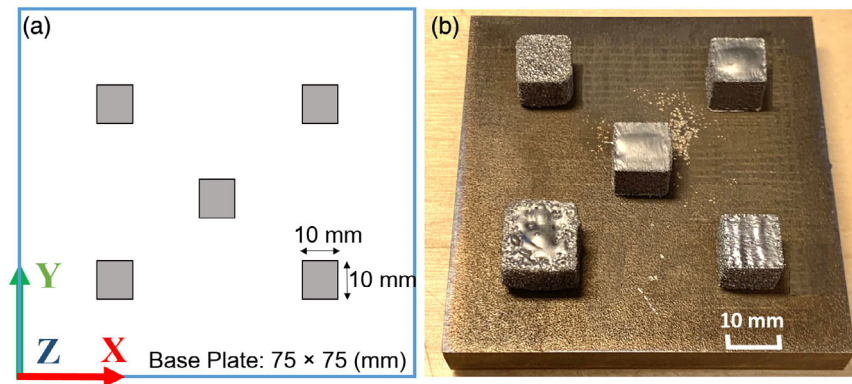


Figure 1. a) Density cube layout and setup and b) photo of as-built NiTi density cubes example.

Table 1. Full experiment factorial design of scan speed and beam current.

Sample no.	Beam current [mA]	Scan speed [mm s ⁻¹]	Cooling condition	Linear energy [J m ⁻¹]
1	5	1,000	Slow	300.0
2	5	1,250	Slow	240.0
3	5	1,500	Slow	200.0
4	5	2,500	Slow	120.0
5	10	6,000	Slow	100.0
6	10	7,000	Slow	85.7
7	10	9,000	Slow	66.7
8	15	7,000	Slow	128.6
9	20	7,000	Slow	171.4
10	25	7,000	Slow	214.3
11	5	2,000	Medium	150.0
12	10	5,000	Medium	120.0
13	10	8,000	Medium	75.0

Figure 2a is showing the temperature profile of the slow cooling in the vacuum and Figure 2b is the temperature profile of replenishing with helium to achieve a medium cooling rate. For the first two builds of samples 1–9, with the vacuum slow cooling, the cooling time to 100 °C was approximately 5 h. While for the third build, samples 10–13 with the helium medium cooling had the cooling time of 1.5 h to the 100 °C. Typical manufactured density cubes are demonstrated in Figure 1b.

According to Karimi et al.,^[20] the linear energy input (J m⁻¹) is a measure for the averaged applied energy onto the material for a single track of scanning; see Equation (1). The calculation of linear energy input per single track is the ratio between the power of the electron beam and the scanning speed.

$$\text{Linear energy input (J m}^{-1}\text{)} = \frac{\text{Voltage (V)} \times \text{Current (A)}}{\text{Scanning speed (m s}^{-1}\text{)}} \quad (1)$$

The density of the cubes was measured using Archimedes' principle (ASTM B311-17).^[21] For the measurements using Archimedes' principle, the weighing liquid was isopropanol 99.5% with a density of 0.786 g cm⁻³. The isopropanol 99.5% was used instead of water since it has better access to the rough surfaces of PBF-EB parts and hence it can provide more accurate density data.^[22] The average of three measurements was taken as the mean value. For geometrical mismatch, the cross-section of each sample was calculated after measuring the X–Y dimensions using a caliper. The mean value was reported from an average of three measurements. This was compared to the dimensions in the CAD model.

Three samples with the highest relative density were chosen for further analysis: samples 1, 10, and 11. These samples were produced using a slow scan speed and vacuum slow cooling (LP-VC), high power with high scan speed and vacuum slow cooling (HP-VC), and low power with low speed and helium medium cooling (LP-HC), respectively. The high power with high scan speed and helium medium cooling (HP-HC) was not considered for further analysis since the part's geometrical mismatch was too large while the relative density was too low.

The microstructure of polished X–Z cross sections of each sample was revealed by Zeiss ultra 55 scanning electron microscope (SEM, Zeiss, Germany) which is equipped with Oxford

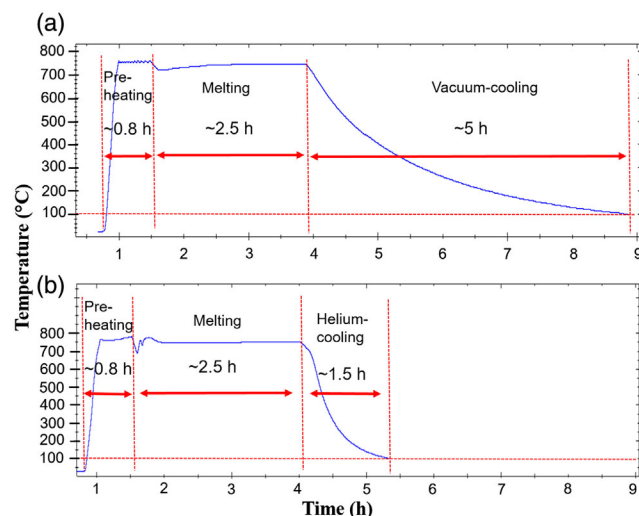


Figure 2. The build temperature profile for the bottom of the start plate with two different cooling conditions: a) slow vacuum cooling, and b) medium helium atmosphere cooling.

Instruments energy dispersive spectroscopy (EDS) and electron backscattered diffraction (EBSD) detector. Oxford Instruments Aztec and HKL Channel 5 software were used to analyze the EBSD data. The phase transformation temperature of the gas atomized powder and as-built samples were measured by differential scanning calorimetry (DSC, Mettler Toledo, USA) with a heating-and-cooling rate of 10 K min^{-1} between -80 to 130°C under flowing nitrogen. The testing specimen was cut from the top corner of the cubes and each specimen was characterized two times to obtain repeatable results.

The phase fractions of the powder and samples were conducted at room temperature (22°). A Bruker D8 Discover X-ray diffractometer (XRD, Bruker, USA) with copper $K\alpha$ radiation was used to investigate the phases present near the middle part of the samples along the build direction. Microcompression testing was carried out on approximately $3 \times 3 \times 5 \text{ mm}^3$ samples at room temperature (RT). This was carried out inside SEM using a Deben microtest stage with a strain rate of $3 \times 10^{-4} \text{ s}^{-1}$. The Deben microcompression testing device's software records the load and the compression. Due to the limit of the maximum load

and the size of the samples, the stress applied in this experiment has a limitation of 600 MPa.

3. Results and Discussion

3.1. Process Parameter Optimization

Figure 3 shows the densities of the manufactured parts as a function of electron beam linear energy density. As expected, the part density increases with increasing linear energy density until densities over 98% are reached. However, by simultaneously looking at the parameters in Table 1, it can be appreciated that linear energy density is not the only influential factor, as higher scan speed and higher beam current typically lead to a lower relative density even at the similar linear energy density. For example, although sample 9 has been made with slightly higher linear energy input than sample 11, sample 11 is still denser due to the use of a lower scan speed and a lower beam current. This higher beam current in conjunction with a higher scan speed presumably results in the lower density. This could be due to the larger beam diameter on the focal plane at higher beam currents,^[23] which creates a stronger negative repulsive force between the electrons due to the higher number density of electrons.^[24] The larger beam diameter increases the melt pool size, which in turn increases the recoil pressure and Marangoni flow, so that the melt pool turbulence and heat losses increase, creating defects such as keyholes.^[25]

In addition, the dimensional mismatch of manufactured parts with the used CAD model is another important variant, which should be studied with respect to the energy input, as well as the beam current. As shown in Figure 4a, no clear trend can be found for the dimensional mismatch of the parts when compared to the linear energy input. However, in Figure 4b, it is evident that a higher applied beam current directly increases the dimensional mismatch of the parts. This is again due to the high beam current which increases the electron beam spot and the melt pool sizes. Consequently, the larger melt pool pushes the melt boundaries into the surrounding powder and increases the part size. Although to solve this issue one can consider compensating for it when the designing the part for the

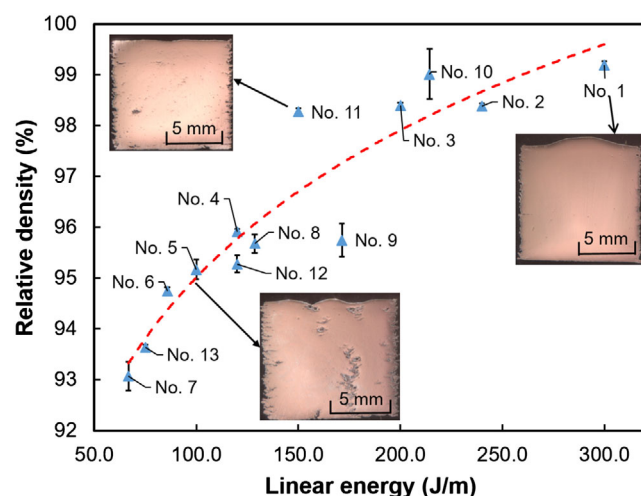


Figure 3. The relative density versus the linear energy density of the parts.

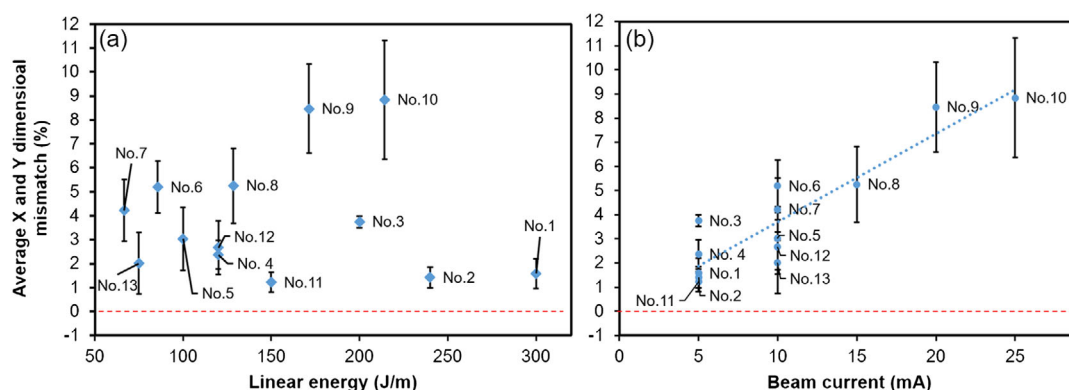


Figure 4. Average X and Y dimensional mismatch between the manufactured parts and the CAD model in relation to a) the linear energy density and b) the beam current.

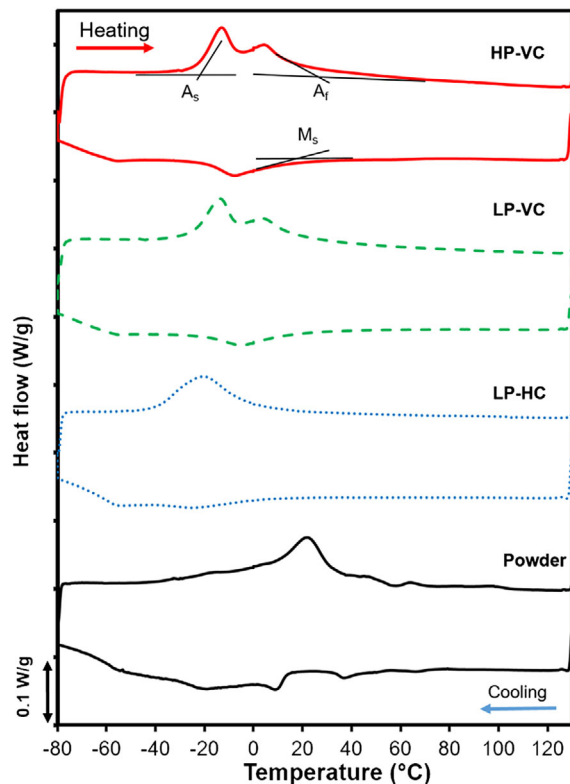


Figure 5. DSC curves of NiTi samples showing the phase transformation along the temperature change.

electron beam spot size, a low beam current is still favorable to keep the parts' geometrical accuracy.

3.2. Phase Transformation

Figure 5 shows the DSC curves, illustrating the phase transformation temperature of powder and as-built parts. The DSC curve of the powder reveals apparent serrations perhaps due to 1) inhomogeneity in the powder chemical compositions and 2) multistep martensitic transformation of B2 (austenite) \rightarrow R \rightarrow B19' (martensite) during the cooling process. However, it is noted that the curves for the as-built parts show less serration than that from the powder. This indicates that PBF-EB can mitigate the inhomogeneity (for instance the local change in composition, crystalline size, etc.) of the powder. However, multistep martensitic transformation can still remain after PBF-EB due to the precipitation (e.g., Ni_4Ti_3) occurring due to the high PBF-EB processing temperature and slow cooling.

The LP-VC and HP-VC samples demonstrated a very comparable DSC transformation, perhaps due to their similar cooling rate (on average $2.1^\circ\text{C min}^{-1}$). This included a two-step austenitic transformation of B19' \rightarrow R \rightarrow B2 during the heating process and multistep B2 \rightarrow R \rightarrow B19' martensitic transformation during cooling. According to **Figure 6**, the phase transformation temperature for sample LP and HP is similar, which suggests that the energy input, scan speed, and beam current is not the main influential factor on the as-built parts' phase

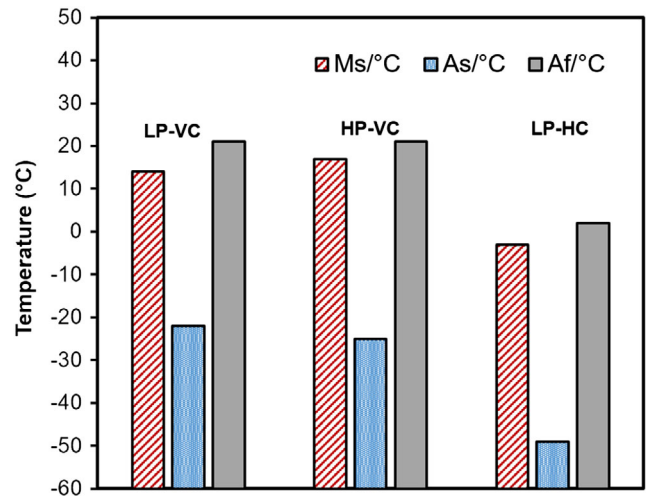


Figure 6. Phase transformation temperature of as-built NiTi samples.

transformation temperature. This result is consistent with the result of Ren et al.^[16] However, this vacuum cooling in PBF-EB process has a similar effect to an aging process. This leads to the formation of Ni-rich intermetallic compounds, e.g., Ni_4Ti_3 , which promote the formation of R-phase and hence a multistep transformation. This is since an initial martensitic transformation from higher temperature B2 phase to an intermediate R-phase followed by a transformation to B19' occurs in several stages as the kinetic barrier of the R-phase is lower than the formation of the martensite phase.^[26] At the same time, the formation of the Ni-rich intermetallic compounds can consume some of the Ni elements in the material, which can lower the Ni-ratio in the matrix.

In comparison, sample LP-HC (cooled with $6.9^\circ\text{C min}^{-1}$ on average) exhibits a one-step phase transformation which is B19' \rightarrow B2 austenitic transformation during heating and a multistep phase transformation B2 \rightarrow R and R \rightarrow B19' martensitic transformation during cooling. Moreover, the M_s temperature for medium cooling sample is about 20°C lower than the sample LP-VC and HP-VC. This result agrees with Elahinia et al.^[2] and Hamilton et al.^[26] that a longer aging period can elevate the transformation temperatures due to the formation of precipitates. Thus, a shorter cooling time can suppress the formation of Ni-rich precipitate, which equivalently increases the Ni ratio in the matrix compared to the vacuum slow-cooled samples.

PBF-EB as a "hot-process" is distinct even from other powder bed processes, such as PBF-LB. Since PBF-EB has a rather long cooling time up to 1–10 h depending on the material, build size, and cooling mode, it is very likely to lead to some aging. There is some Ni-rich precipitation (e.g., Ni_4Ti_3) or Ti-rich inclusions formed spontaneously depending on the postcooling rate, which consumes the Ni or Ti element from the matrix. In turn, the Ni-ratio in the matrix was changed respectively. It is important to note that the cooling rate after the build plays a more important role in as-built parts' phase transformation temperature than manufacturing parameters, such as beam current and beam speed. The phase transformation temperature of NiTi alloy decreases with increasing cooling rate.^[27] Moreover, decreasing

the cooling rate introduces incoherency stress and increases the A_f temperature. Since the Ni concentration of the matrix is reduced due to the formation of the Ni-rich intermetallic compounds, for instance, Ni_4Ti_3 and Ni_3Ti , which also facilitates multistep phase transformations.^[24,25] However, the formation of Ti-rich precipitate such as Ti_4Ni_2O/Ti_2Ni can cause a decrease in M_s temperature due to the increasing of the Ni content.^[28] Nevertheless, according to Frenzel et al.^[28] relating the M_s temperature to Ni content in the matrix, the Ni ratio in the matrix could be estimated to be ≈ 50.4 at% for the vacuum cooling groups. In comparison, the M_s temperature for the helium cooling sample is a bit less. This means that the Ni ratio in the matrix of this part could be a bit higher perhaps around 50.6 at%.

3.3. Phase Identification

The XRD pattern of as-built NiTi samples in comparison with the powder is shown in Figure 7. For the scans of powder, the indexed peaks corresponding to the cubic $Pm\bar{3}m$ space group: $(110)_{B2}$, $(200)_{B2}$, $(211)_{B2}$, $(220)_{B2}$, and $(310)_{B2}$ suggest that the austenitic B2 NiTi phase is dominant. In addition, minor nickel titanium monoclinic P21/m (martensite) peaks were also detected in the powder. Similarly, austenite B2 NiTi is dominant in all as-built samples.

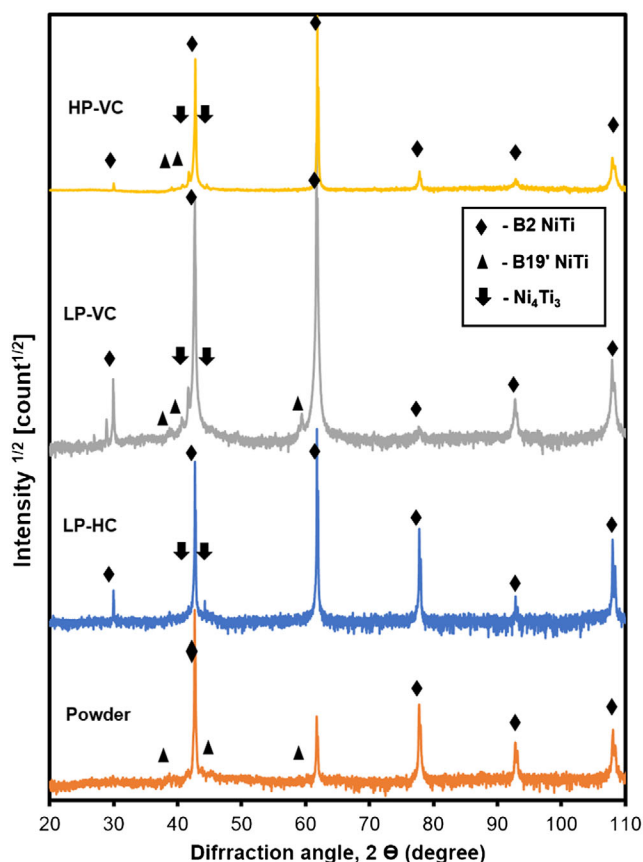


Figure 7. XRD pattern of as-received powder, recycled powder, and as-built samples along building direction.

Within as-built samples, minor B19' martensitic phases were also identified, particularly in samples LP-VC and HP-VC (Figure 7). This is consistent with the DSC result as LP-HC has the M_s temperature below 0 °C while the M_s temperature for the slow-cooling sample is around 15 °C, therefore, it is reasonable that the slow-cooled samples would form a small amount of martensitic phase when cooled to a temperature around room temperature (20 °C), while the fast-cooled sample would not. Moreover, Ni_4Ti_3 seems to exist in all the samples (similar to reports in the study of Zhou et al.^[15] for as-built parts). Nevertheless, slow cooling clearly promotes the formation of these precipitates compared to the helium cooling, according to their corresponding peak intensity. This indicates decreasing the cooling rate increases the amount of Ni_4Ti_3 precipitates. The existence of Ni_4Ti_3 in XRD is in agreement with the DSC phase transformations in Figure 5. Based on the result of Ren et al.,^[29] R phase can be induced by aging the Ni-rich NiTi alloys to produce the fine Ni_4Ti_3 precipitate, causing a multistage transformation. While the parent B2 transforms to B19' phase directly in quenched Ni-Ti binary alloys.

3.4. Microstructural Characterization of As-Built NiTi Samples

In Figure 8, there are several distinct microstructural characteristics correlated with the beam current, scanning speed, and the cooling rate. As seen, a columnar grain structure is observed along the build direction in all samples, corresponding to the thermal gradient direction. In the vacuum cooling group, Figure 8a–c and e–g, the sample HP shows coarser columnar grains compared to the LP sample. This can be attributed to the larger beam current intensity compared to the LP case (25 mA vs. 5 mA), which generates a larger beam and, hence, melt pool (this can also be seen as larger geometrical mismatch in Figure 4). The larger melt pool reduces the thermal gradient, causing less fragmentation in dendrites as well as a smaller undercooling, which results in fewer solid nuclei becoming stable in the melt pool, and, so leads to fewer, coarser grains.^[30] Moreover, it seems that there are more Ti-rich precipitates (seen as small black dots) close to the grain boundaries in Figure 8c,g, while there are fewer same precipitates in the grain boundaries of LP-HC (Figure 8k). This could be because of the slow vacuum cooling rate after the fabrication allowing the precipitates to grow at the grain boundaries during the cooling stage as compared to the medium cooling rate achieved using helium gas.^[31]

Moreover, it can be observed that as-built samples exhibit a strong texture for all three samples shown in the pole figures (Figure 8d,h,l). This can be associated to the imposed thermal gradient during PBF-EB which is dominant $\langle 100 \rangle$ texture along the build direction. This result is well consistent with our XRD spectrum (Figure 7) that a (200) peak with a high intensity. Besides, the sample HP-VC has the maximum pole intensity along the build direction compared to the LP samples since the high power of the EB leads to a more profound thermal influence over the previous layers that can reduce the misalignment between grain orientations on the build direction. In addition, vacuum slow cooling seems to contribute to the alignment between grain orientations due to a longer rearrangement time.

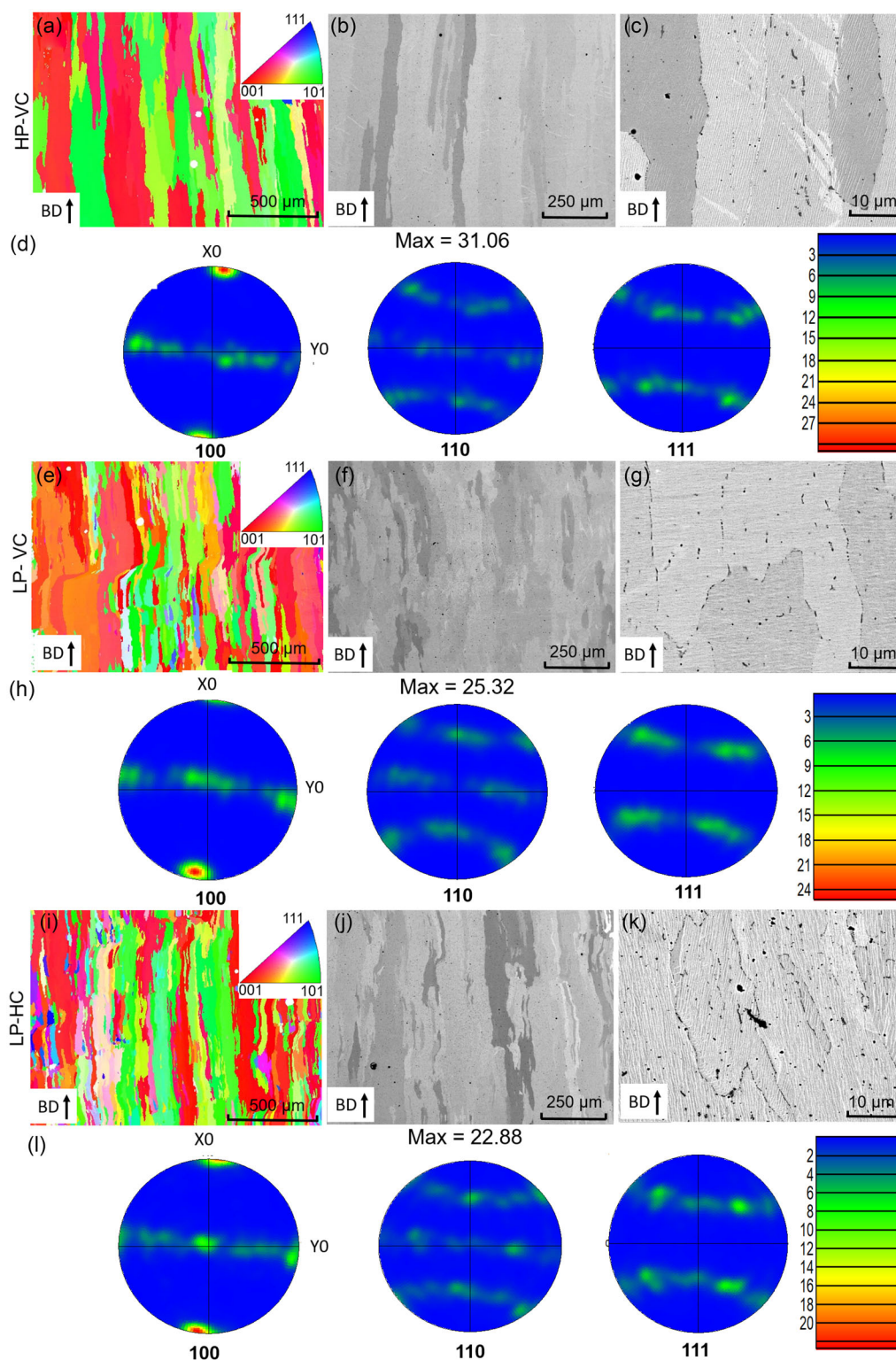


Figure 8. EBSD, SEM images, and pole figures of microstructures along X–Z plane or build section. EBSD images of a) high power, vacuum slow cooling. e) Low power, slow cooling. i) Low cooling, helium medium cooling samples. SEM images of b,c) high power, vacuum slow cooling. f,g) low power, slow cooling. j,k) low cooling, helium medium cooling samples. Pole figure of d) high power, vacuum slow cooling. h) Low power, slow cooling. l) Low cooling, helium medium cooling samples.

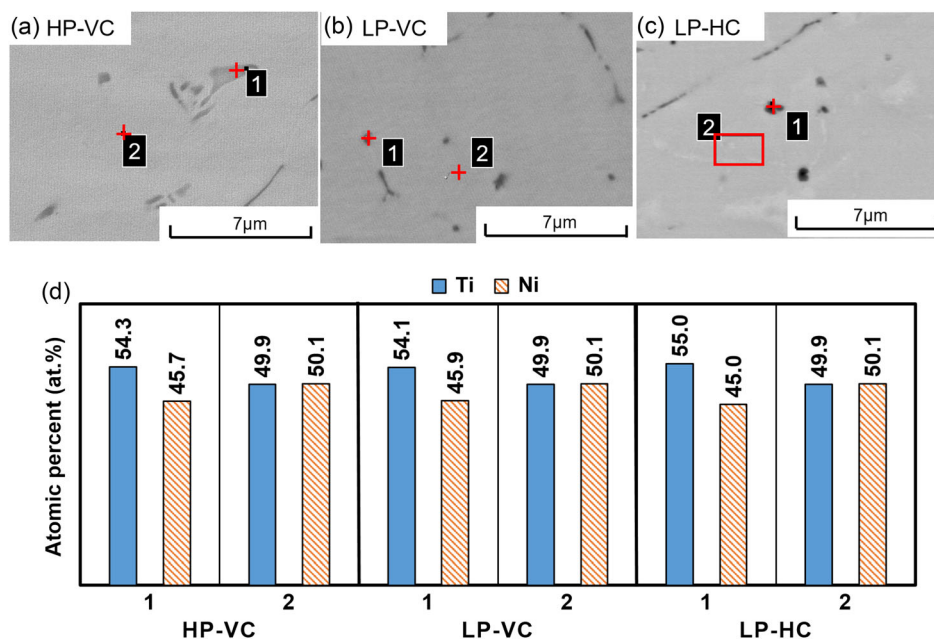


Figure 9. EDS results of as-built samples a). High power, slow vacuum cooling b). Low power, slow vacuum cooling c). Low power, helium medium cooling d). Atomic percent comparison of Ti and Ni elements at chosen points.

From the EDS mapping in **Figure 9**, the chemical compositions of the matrix and in regions that include large precipitates have been identified. It is obvious that for all as-built samples, the matrix has a near-equiatomic composition. Besides, titanium-rich inclusions were identified in all three samples. It is not possible to determine the absolute composition of these precipitates, as they are smaller than the region in which X-rays are likely to be generated in the mapping. However, the signal will be a combination of X-rays generated in the precipitate itself and the surrounding matrix. The signals in regions centered on precipitates show an elevated titanium content, which suggests that the precipitates contain higher amounts of titanium than the matrix. These titanium-rich inclusions have also been reported previously by many researchers.^[28,32,33] Since Ti_2Ni is thermodynamically stable above 1,050 °C, the formation of titanium-rich inclusion probably occurs during the PBF-EB melting stage and/or the production of the powder stock.^[16,34] These titanium-rich inclusions influence the phase transformation temperature by increasing the nickel content in the matrix and hence decreasing the transformation temperature.^[28]

3.5. Cyclic Compression Test of As-Built PBF-EB Samples

Figure 10 shows the compression behavior of the as-built samples made by LP-VC, HP-VC, and LP-HC. It is noted that after reaching around 600 MPa of compressive stress, the strain in all samples reaches around 8%. However, the behavior of different samples is rather distinct. As seen, the plateau is most noticeable in LP-HC, attributed to reduced precipitation nucleation and precipitation growth as a result of the faster cooling. In addition, an obvious plateau is observed for LP-VC sample while there is no clear plateau for the HP-VC sample even though these samples have similar A_f temperature. This plateau occurs due to the

phase transformation from the austenite to the martensite, decreasing the strength growth rate of the material during the transformation period. In other words, one may need less load to deform the material during twinning to form martensite. Therefore, the plateau can be observed until the elastic deformation of its martensite phase starts.^[35] The critical stress for inducing martensite (σ_M) is around 400 MPa for LP-VC part while the σ_M is around 200 MPa for the LP-HC sample. Also, this is in agreement with previous XRD results that LP-VC exhibits prominent Ni_4Ti_3 peaks (Figure 7) as well as the higher transformation temperatures for vacuum cooling (Figure 5). This can be related to the slow vacuum cooling for the sample which increases the critical stress for inducing the martensitic transformation due to the Ni_4Ti_3 precipitation.^[28,29] Compared to slow vacuum cooling, medium helium cooling leads to less precipitation, which lowers σ_M (compare Figure 10a–c).

For the HP-VC sample, there is no clear plateau and σ_M . This implies the elastic modulus of the austenite is close to the apparent modulus for the martensitic transformation.^[35] This could be due to the formation of fine Ni_4Ti_3 precipitates under vacuum cooling, causing precipitation hardening that may pin the martensite twins and hence increases the modulus necessary for martensitic detwinning.^[27] In addition, σ_M is decreasing with an increasing number of cycles. This could be due to the internal stresses from small amounts of slip deformation that can assist the martensite transformation.^[36] In contrast, all the samples have shown a recoverable strain over 7% despite very small and rather negligible amount of the irreversible stain being observed in each cycle. This can be once again attributed to the formation of a small amount of martensite which gives a residual strain that is accommodated by plastic deformation via slip.^[35] This slip is inhibited by the presence of precipitates, and so due to increased precipitation, the slow vacuum cooling

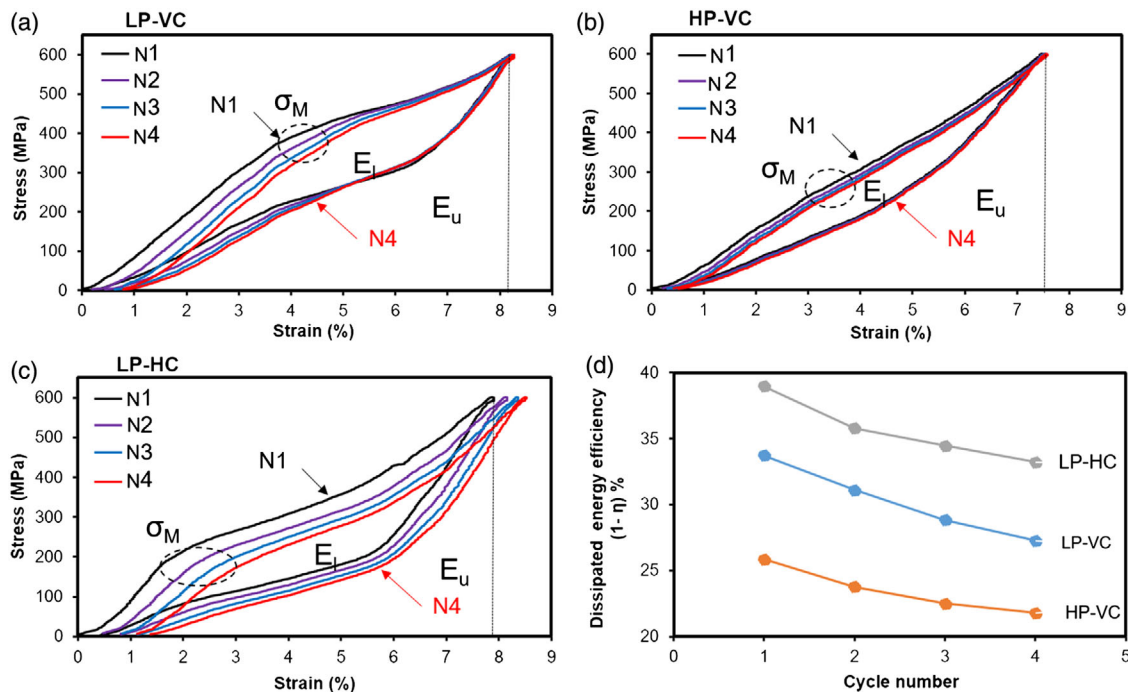


Figure 10. Cyclic compressive behavior of as-built NiTi samples with different manufacturing parameters along the build direction. a) Part fabricated with low power and slow vacuum cooling (LP-VC), b) part fabricated with high power and slow vacuum cooling (HP-VC), c) part fabricated with low power and medium helium cooling rate (LP-HC). d) The dissipated energy efficiency ($1-\eta$) of as-built NiTi samples.

samples exhibit less irreversible strain accumulation over medium helium cooling samples, which implies that these samples will exhibit less martensite with a residual strain accommodated by plastic deformation under this imposed condition.^[37]

The area within the loading (E_L) and unloading (E_U) stress-strain hysteresis loop gives for the heat energy dissipated per unit volume (i.e., E_L-E_U). Therefore, the ratio of E_U/E_L is the efficiency for elastic energy storage, η .^[36] Accordingly, the dissipation of energy in this material is $1-\eta$, which can represent the damped energy within the corresponding loading-unloading cycle (as shown in Figure 10d). As seen, the LP-HC sample demonstrates the highest energy dissipation, otherwise known as the damping energy. This high damping property is attributed to the gradual formation of the martensite, altering the internal fraction (IF) between the interfaces (martensite variant interface, twin boundary). According to the measurement from Van Humbeeck et al.,^[6] the IF of near equiatomic NiTi alloy reaches a peak with increasing the annealing temperature (which was 550 °C in the mentioned work) and then reduces again. The formation of this IF peak was related to the contribution of fine coherent or partially coherent precipitates formed from the annealing at this condition. Accordingly, it can be postulated that the medium helium cooling also creates a condition that forms fine coherent or partially coherent precipitates, while in comparison vacuum slow cooling coarsens the precipitates above these optimum sizes as compared to the higher annealing temperatures above 550 °C before. This concept of using different PBF-EB parameters (e.g., postcooling rate) to reach different dissipated energy can be used to manipulate the damping performance in damping applications.^[38]

It is worth mentioning that the parts were compressed inside SEM to visualize the reversible austenite to martensite transformation. However, since this was not possible due to the lower-than-required resolution of this technique, the authors just used the mechanical data without providing the very poor microstructural visualization that they received.

4. Conclusions

- 1) The part density increases with increased linear energy density until dense parts are reached.
- 2) At the same level of the energy input, low beam current and low scan speed led to a denser part than that from using a high beam current and high scan speed. This was attributed to the slight smoke or spattering caused by the repulsive electrostatic forces from the larger electron beam current.
- 3) The higher beam current also increased the part size and hence the geometrical mismatch of the as-built parts. This was attributed to the increase of the EB spot size with the increase of beam current.
- 4) The electron beam power affects the microstructure and grain size of the part. This, in turn, had a small impact on the shape memory response.
- 5) Instead of EB process parameters, postcooling rate was found to be the controlling factor on the NiTi phase transformation temperature. This was attributed to the Ni₄Ti₃ precipitation which is highly dependent on the postcooling rate. In general, the slower cooling rate resulted in higher A_f and M_s temperatures and a wider phase transformation window than those from the parts with the medium cooling rate.
- 6) Ti-rich inclusions and Ni₄Ti₃ were detected in the part produced by PBF-EB.
- 7) In

general, as-built parts exhibited a good pseudoelasticity in the compression test with a near 8% recoverable strains.

Acknowledgements

The authors acknowledge the financial support provided by Sustainable Industry and Society (IRIS) and the Excellence in Production Research (XPRES) at KTH.

Conflict of Interest

The authors declare no conflict of interest.

Data Availability Statement

The data that support the findings of this study are available from the corresponding author upon reasonable request.

Keywords

cooling rate, mechanical property, NiTi, PBF-EB, process parameter

Received: December 16, 2022

Revised: April 9, 2023

Published online:

- [1] S. Parvizi, S. M. Hashemi, F. Asgarinia, M. Nematollahi, M. Elahinia, *Prog. Mater. Sci.* **2021**, 117, 100739.
- [2] M. Elahinia, N. Shayesteh Moghaddam, M. Taheri Andani, A. Amerinatanzi, B. A. Bimber, R. F. Hamilton, *Prog. Mater. Sci.* **2016**, 83, 630.
- [3] J. Mohd Jani, M. Leary, A. Subic, M. A. Gibson, *Mater. Des.* **2014**, 56, 1078.
- [4] P. Kumar, U. V. Waghmare, *Materialia* **2020**, 9, 100602.
- [5] K. Vanmeensel, K. Lietaert, B. Vrancken, S. Dadbakhsh, X. Li, J. P. Kruth, P. Krakhmalev, I. Yadroitsev, J. Van Humbeeck, *Additively Manufactured Metals for Medical Applications*, Elsevier **2018**, <https://doi.org/10.1016/B978-0-12-812155-9.00008-6>.
- [6] J. Van Humbeeck, *J. Alloys Compd.* **2003**, 355, 58.
- [7] J. H. Schiavon Mota, E. B. Lara Rosa, J. V. Carvalho Fontes, S. B. Shiki, P. Gargarella, C. E. Hirata Ventura, A. F. Sette Antonialli, *Procedia CIRP* **2022**, 108, 519.
- [8] R. Kuppuswamy, A. Yui, *Int. J. Adv. Manuf. Technol.* **2017**, 93, 11.
- [9] M. H. Elahinia, M. Hashemi, M. Tabesh, S. B. Bhaduri, *Prog. Mater. Sci.* **2012**, 57, 911.
- [10] S. Dadbakhsh, M. Speirs, J. P. Kruth, J. Schrooten, J. Luyten, J. Van Humbeeck, *Adv. Eng. Mater.* **2014**, 16, 1140.
- [11] M. Speirs, X. Wang, S. Van Baelen, A. Ahadi, S. Dadbakhsh, J. P. Kruth, J. Van Humbeeck, *Shape Mem. Superelasticity* **2016**, 2, 310.
- [12] C. Körner, *Int. Mater. Rev.* **2016**, 61, 361.
- [13] Z. Lin, S. Dabakhsh, A. Rashid, *J. Manuf. Processes* **2022**, 83, 180.
- [14] M. D. Hayat, G. Chen, S. Khan, N. Liu, H. Tang, P. Cao, *Key Eng. Mater.* **2018**, 770, 148.
- [15] Q. Zhou, M. D. Hayat, G. Chen, S. Cai, X. Qu, H. Tang, P. Cao, *Mater. Sci. Eng., A* **2019**, 744, 290.
- [16] D. Ren, H. Zhang, X. Zhao, F. Wang, W. Hou, S. Wang, S. Li, W. Jin, R. Yang, *Acta Metall. Sin.* **2020**, 56, 1103.
- [17] C. Wang, X. P. Tan, Z. Du, S. Chandra, Z. Sun, C. W. J. Lim, S. B. Tor, C. S. Lim, C. H. Wong, *J. Mater. Process. Technol.* **2019**, 271, 152.
- [18] X. Zhao, S. Dadbakhsh, A. Rashid, *J. Manuf. Process.* **2021**, 62, 418.
- [19] C. J. Smith, F. Derguti, E. Hernandez Nava, M. Thomas, S. Tammawilliams, S. Gulizia, D. Fraser, I. Todd, *J. Mater. Process. Technol.* **2016**, 229, 128.
- [20] P. Karimi, E. Sadeghi, J. Ålgårdh, J. Andersson, *Mater. Charact.* **2019**, 148, 88.
- [21] ASTM B311-17, *ASTM Int.* **2017**, 1, <https://doi.org/10.1520/B0311-17.2>.
- [22] A. B. Spierings, M. Schneider, R. Eggenberger, *Rapid Prototyping J.* **2011**, 17, 380.
- [23] Z. Lin, X. Zhao, S. Dadbakhsh, A. Rashid, in 14th Lamdamap Conf. **2021**.
- [24] B. von Brömssen, *Electron Beam Welding of Thick Copper Material*, SKI **2002**.
- [25] M. Mollamahmutoglu, O. Yilmaz, R. Unal, B. Gumus, E. Tan, *Int. J. Adv. Manuf. Technol.* **2022**, 120, 4041.
- [26] R. F. Hamilton, T. A. Palmer, B. A. Bimber, *Scr. Mater.* **2015**, 101, 56.
- [27] K. Otsuka, X. Ren, *Prog. Mater. Sci.* **2005**, 50, 511.
- [28] J. Frenzel, E. P. George, A. Dlouhy, C. Somsen, M. F. X. Wagner, G. Eggeler, *Acta Mater.* **2010**, 58, 3444.
- [29] X. Ren, N. Miura, J. Zhang, K. Otsuka, K. Tanaka, M. Koiwa, T. Suzuki, Y. I. Chumlyakov, M. Asai, *Mater. Sci. Eng., A* **2001**, 312, 196.
- [30] H. E. Helmer, C. Körner, R. F. Singer, *J. Mater. Res.* **2014**, 29, 1987.
- [31] B. Karbakhsh Ravari, S. Farjami, M. Nishida, *Acta Mater.* **2014**, 69, 17.
- [32] J. Michutta, C. Somsen, A. Yawny, A. Dlouhy, G. Eggeler, *Acta Mater.* **2006**, 54, 3525.
- [33] J. Khalil Allafi, X. Ren, G. Eggeler, *Acta Mater.* **2002**, 50, 793.
- [34] C. L. Chu, J. C. Chung, P. K. Chu, *Trans. Nonferrous Met. Soc. China* **2006**, 16, 49.
- [35] H. Sehitoglu, I. Karaman, R. Anderson, X. Zhang, K. Gall, H. J. Maier, Y. Chumlyakov, *Acta Mater.* **2000**, 48, 3311.
- [36] S. Miyazaki, T. Imai, Y. Igo, K. Otsuka, *Metall. Trans. A* **1986**, 17, 115.
- [37] S. Saedi, A. S. Turabi, M. T. Andani, C. Haberland, H. Karaca, M. Elahinia, *J. Alloys Compd.* **2016**, 677, 204.
- [38] X. Wang, M. Speirs, S. Kustov, B. Vrancken, X. Li, J. P. Kruth, J. Van Humbeeck, *Scr. Mater.* **2018**, 146, 246.